



Electrospinning preparation of one-dimensional Co^{2+} -doped $\text{Li}_4\text{Ti}_5\text{O}_{12}$ nanofibers for high-performance lithium ion battery

Xueyang Ji¹ · Dong Li¹ · Qifang Lu¹ · Enyan Guo¹ · Linbing Yao¹ · Hao Liu¹

Received: 13 November 2017 / Revised: 28 December 2017 / Accepted: 12 January 2018 / Published online: 20 January 2018
© Springer-Verlag GmbH Germany, part of Springer Nature 2018

Abstract

One-dimensional Co^{2+} -doped $\text{Li}_4\text{Ti}_5\text{O}_{12}$ nanofibers with a diameter of approximately 500 nm have been synthesized via a one-step controllable electrospinning method. The Co^{2+} -doped $\text{Li}_4\text{Ti}_5\text{O}_{12}$ nanofibers were systematically characterized by XRD, ICP, TEM, SEM, BET, EDS mapping, and XPS. Based on the cubic spinel structure and one-dimensional effect of $\text{Li}_4\text{Ti}_5\text{O}_{12}$, Co^{2+} -doped $\text{Li}_4\text{Ti}_5\text{O}_{12}$ nanofibers exhibit the enlarged lattice volume, reduced particle size and enhanced electrical conductivity. More importantly, Co^{2+} -doped $\text{Li}_4\text{Ti}_5\text{O}_{12}$ nanofibers as a lithium ion battery anode electrode performs superior electrochemical performance than undoped $\text{Li}_4\text{Ti}_5\text{O}_{12}$ electrode in terms of electrochemical measurements. Particularly, the reversible capacity of Co^{2+} -doped $\text{Li}_4\text{Ti}_5\text{O}_{12}$ electrode reaches up to 140.1 mAh g^{-1} and still maintains 136.5 mAh g^{-1} after 200 cycles at a current rate of 5 C. Therefore, one-dimensional Co^{2+} -doped $\text{Li}_4\text{Ti}_5\text{O}_{12}$ nanofiber electrodes, showing high reversible capacity and remarkable recycling property, could be a potential candidate as an anode material.

Keywords $\text{Li}_4\text{Ti}_5\text{O}_{12}$ nanofibers · Electrospinning · Co^{2+} -doped · Lithium ion battery

Introduction

In recent years, lithium ion batteries (LIBs), as one of the most popular energy storage systems (ESSs), due to its long lifetime, high energy efficiency, and competitive energy density [1–3], have received increasing research interests to tackle issues of energy insufficiency and environmental pollution caused by vast fossil fuel consumption. As one of the most promising anode materials for LIBs, the spinel $\text{Li}_4\text{Ti}_5\text{O}_{12}$ (denoted as LTO) nanomaterials have attracted tremendous attention owing to the high lithium insertion/extraction voltage (~1.55 V, vs Li^+/Li), zero volume change during the charge/discharge process, and low material cost [4–6]. However, like many other electrode materials, LTO-based anodes are

plagued with two main challenges: the low electrical conductivity and poor lithium ion diffusion coefficient [7, 8].

In order to tackle these challenges, various strategies have been investigated for the modified LTO anode material, such as carbon coating, nanostructure designing, and nonmetal ions and metal ions doping [9–12]. As is known to all, one-dimensional (1D) nanostructure could prevent the aggregation of particles [13], which could make full use of the advantages of the nanostructures to offer a large number of active sites for Li^+ ions, improve the intercalation kinetics, and reduce the diffusion pathways to improve electrochemical properties, such as reversible capacity and rate capability [13, 14]. Meanwhile, the electrospinning, as a simple and low-cost technology, is chosen as the synthetic method to fabricate the continuous 1D novel nanostructures, such as nanofibers, microfibers, nanotubes, and nanobelts as electrode materials for LIBs [15–18]. Furthermore, metal ion doping can be chosen to improve the insulating character owing to the superior maneuverability and favorable effects. Consequently, various metal ion doping approaches have been proposed in the case of doping with Cr^{3+} [12], Sc^{3+} [19], Dy^{3+} [20], and Ce^{3+} [21]. Nevertheless, metal ion doping combining electrospinning method to prepare the modified LTO electrode has been rarely investigated, except Ni^{3+} -doped LTO [22], Zr^{4+} -doped LTO [23], and Cu^{2+} -doped LTO nanofibers [24]. But to the best of

Electronic supplementary material The online version of this article (<https://doi.org/10.1007/s11581-018-2453-2>) contains supplementary material, which is available to authorized users.

✉ Qifang Lu
luqf0110@126.com

¹ Shandong Provincial Key Laboratory of Processing and Testing Technology of Glass and Functional Ceramics, School of Material Science and Engineering, Qilu University of Technology (Shandong Academy of Sciences), Jinan 250353, People's Republic of China

our knowledge, Co^{2+} -doped LTO nanofibers have not been found in the application of lithium ion batteries.

Based on the merits mentioned earlier, 1D Co^{2+} -doped LTO nanofibers have been synthesized via a one-step electrospinning method in the present paper. Introduced Co^{2+} ions into LTO nanofibers, Co^{2+} -doped LTO nanofibers are made up of fine particles and possess lower charge transfer resistance and Li^+ ion diffusion coefficient than pure LTO counterparts.

Experimental

Materials synthesis

All the chemicals were of analytical grade and used as received without further purification.

In a typical synthesis, 0.5000 g polyvinylpyrrolidone (PVP-K90) was dissolved in 10 mL absolute ethanol with magnetic stirring for 12 h at room temperature. Then, 0.4284 g (4.2 mmol) lithium acetate dehydrate ($\text{CH}_3\text{COOLi}\cdot 2\text{H}_2\text{O}$), 1.6676 g (4.9 mmol) tetrabutyl titanate ($\text{C}_{16}\text{H}_{36}\text{O}_4\text{Ti}$), and 0.0291 g (0.1 mmol) cobalt nitrate ($\text{Co}(\text{NO}_3)_2\cdot 6\text{H}_2\text{O}$) were sequentially added into the aforementioned solution. After that, 1 mL acetic acid was successively added to the abovementioned solution in order to avoid the hydrolysis of tetrabutyl titanate. Lithium acetate dehydrate was excessive by 5 wt% to avert the decrease of Li^+ volatilization in the high temperature. The solution was stirred for 12 h to obtain the homogeneous and transparent precursor sols.

The precursor sols were subsequently placed into 20-mL syringe attached to a stainless steel needle with an inner diameter of 0.6 mm, and then ejected from the needle with a voltage of 20 kV. The tip-to-collector distance was set to 20 cm, and aluminum foil was used to collect the electrospun fibers. The flow rate of the precursor sols was 2.26 mL h^{-1} , and the humidity level was maintained around 30% RH. The as-collected gel nanofibers were dried at 80°C for 12 h, and then were put into an air atmosphere programmable muffle furnace calcined to 350°C from room temperature with a heating rate of 1°C min^{-1} for 2 h and then calcined to 800°C at a rate of 2°C min^{-1} for 3 h. The sample was naturally cooled to room temperature in the furnace. Figure 1 shows the schematic illustration of the synthesis of Co^{2+} -doped LTO nanofibers.

Materials characterization

X-ray diffraction (XRD) patterns of the obtained samples were characterized on a Bruker D8 ADVANCE X-ray diffractometer with $\text{Cu K}\alpha$ radiation ($\lambda = 0.15418 \text{ nm}$). Rietveld refinements were carried out using the GSAS program with the EXPGUI interface [25, 26]. Morphologies of the products were identified using scanning electron microscopy (SEM,

Hitachi FESEM-4800) and transmission electron microscopy (TEM, JEM2100). The chemical compositions of the obtained products were analyzed using an inductively coupled plasma optical emission spectroscope (ICP-OES, Optima 7300 DV). The specific surface area measurement was conducted by nitrogen adsorption-desorption experiments (JW-BK100A). X-ray photoelectron spectroscopy (XPS) was performed on a Phi 5300 ESCA system with $\text{Al K}\alpha$ radiation (photoelectron energy 1486.6 eV). The C1s peak at 284.6 eV was used to calibrate peak positions.

Electrochemical measurements

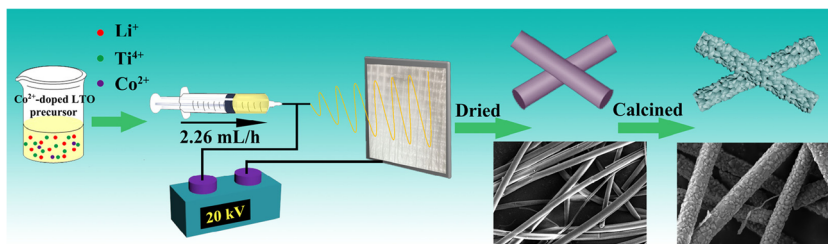
The electrochemical performances of the as-prepared products were evaluated by CR2032 coin-type cells. The working electrode was prepared by blending the as-prepared active material, carbon black, and polyvinylidene fluoride (PVDF) at a weight ratio of 8:1:1 in *N*-methyl-2-pyrrolidone (NMP). The above slurry was then coated onto a Cu foil which was dried at 110°C for 12 h in a vacuum oven. Each working electrode was cut into a disc with a diameter of 1.2 cm, and loading density was 2.0 mg cm^{-2} . The cells were assembled in an Ar-filled glovebox (MIKROUNA) by using lithium foil as the counter electrode and Celgard-2400 polypropylene as the separator. The electrolyte solution was 1 M LiPF_6 dissolved in the mixture of ethylene carbonate and dimethyl carbonate (1:1 volume ratio).

Galvanostatic charge-discharge measurements were tested on a multichannel battery test system (Land CT2001A). Cyclic voltammetry was performed at a scan rate of 0.1 mV s^{-1} from 1.0 to 2.5 V on a computer-controlled CHI760E electrochemical workstation at room temperature. Electrochemical impedance spectroscopy (EIS) patterns were recorded on a CHI760E electrochemical work station with an excitation voltage of 5 mV and a frequency between 100 kHz and 0.01 Hz by using a three-electrode system.

Results and discussion

Figure 2a displays the XRD patterns measured from 10° to 70° 2θ of pure LTO and Co^{2+} -doped LTO nanofibers calcined at 800°C for 3 h, respectively. The diffraction peaks of both samples can be identified as the cubic spinel structure of LTO (JCPDS no. 49-0207), and no impurity phase is found after the introduction of Co^{2+} ions, which illustrates that the doping of Co^{2+} ions does not change the spinel structure of LTO. As shown in Fig. 2b, the magnified (111) peak of Co^{2+} -doped LTO nanofibers shifts to the low angle direction. According to the Bragg equation and Pauling radius, the radius of Co^{2+} (0.745 \AA) is bigger than that of Ti^{4+} (0.605 \AA), so the enlarged lattice parameters could be attributed to Co^{2+} doping into LTO lattice to replace Ti^{4+} . The XRD patterns of

Fig. 1 Synthesis of Co²⁺-doped LTO nanofibers



the increased exposition time have been measured at 2theta from 10° to 120°, and more accurate lattice parameters have been obtained and supplemented in Fig. 2c, d. The convincing lattice volume of Co²⁺-doped LTO nanofibers (584.18 Å³, seen in Fig. 2d) that originated from GSAS atomic structure refinements is larger than that of pure LTO nanofibers (583.67 Å³, shown in Fig. 2c), which corresponds with the results of XRD analysis in Fig. 2b.

Figure 3 shows the morphologies and microstructures of pure LTO and Co²⁺-doped LTO nanofibers. As shown in Fig. 3a, the representative SEM image of LTO precursor nanofibers reveals a host of nondirective and smooth-faced nanofibers with length of up to tens of micrometers, and the diameter is approximately 600 nm. By introducing Co²⁺ ions, there is no obvious change for Co²⁺-doped LTO precursor nanofibers sample which still remains the well-defined and relatively uniform 1D nanostructure. After calcined at 800 °C for 3 h, the pure and Co²⁺-doped LTO nanofibers both possess the uniform diameter (~500 nm) and relatively dense surface (Fig. 3b, e), which are in agreement with the results of TEM analysis (Fig. 3c, f). The diameter reduction after calcination

may be due to the loss of organic components, thermal decomposition of inorganic ions, and crystallization of inorganic oxides [27]. Interestingly, the average size of nanoparticles (~158 nm) made up of Co²⁺-doped LTO nanofibers is smaller than that of pure LTO nanofibers (~186 nm), which may be ascribed to the retarded long-range order of the lattice by introducing doping ions [28]. The reduced particle size for Co²⁺-doped LTO nanofibers could greatly improve the electrochemical kinetics owing to a reduced diffusion length to the fiber core ($t = L^2/D$; t reaction time, L ion diffusion length, D diffusion coefficient) [29]. Moreover, the reduced particle size is beneficial to the increased surface area (shown in Fig. S1) for a fully contact between electrode and electrolyte. EDS mappings of Co²⁺-doped LTO nanofibers in Fig. 3g–i indicate the uniform distribution of the elements of Ti, Co, and O. The element contents of Ti, Co, and O are 31.45, 0.64, and 67.91%, respectively, and the element ratio of Ti and Co is approximately 49.14:1 (shown in Fig. 3j). The ICP-OES analysis for Co²⁺-doped LTO nanofibers in Table S1 further reveals that the element ratio of Ti and Co is about 48.9:1, closing to the initial mole ratio (49:1).

Fig. 2 **a** XRD patterns measured from 10° to 70° 2theta of pure LTO and Co²⁺-doped LTO nanofibers calcined at 800 °C for 3 h, respectively. **b** Enlarged peak of (111) plane of pure LTO and Co²⁺-doped LTO nanofibers, respectively. Rietveld refinements measured from 10° to 120° 2theta of pure LTO (**c**) and Co²⁺-doped LTO (**d**) nanofibers

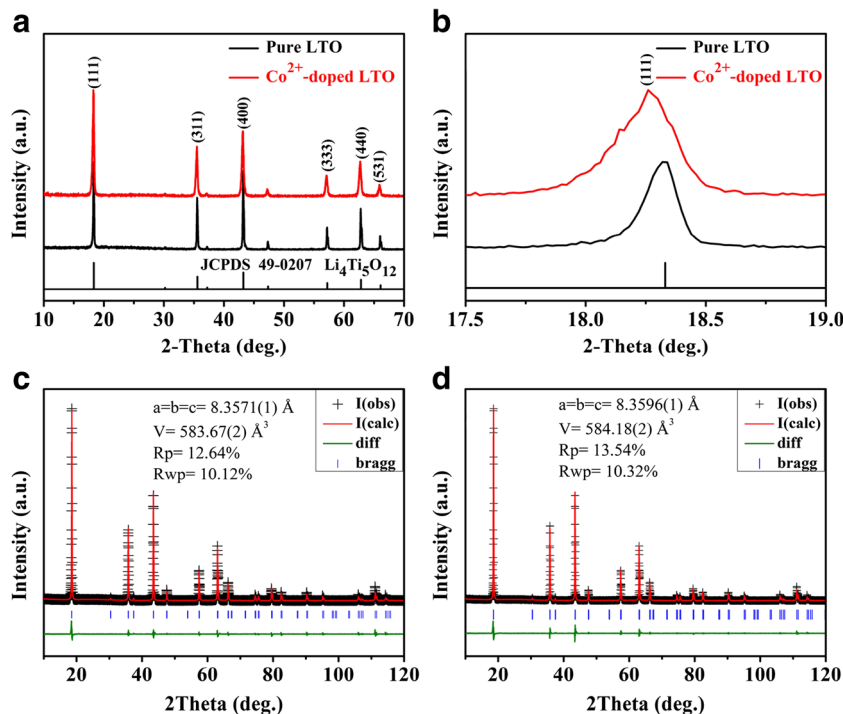
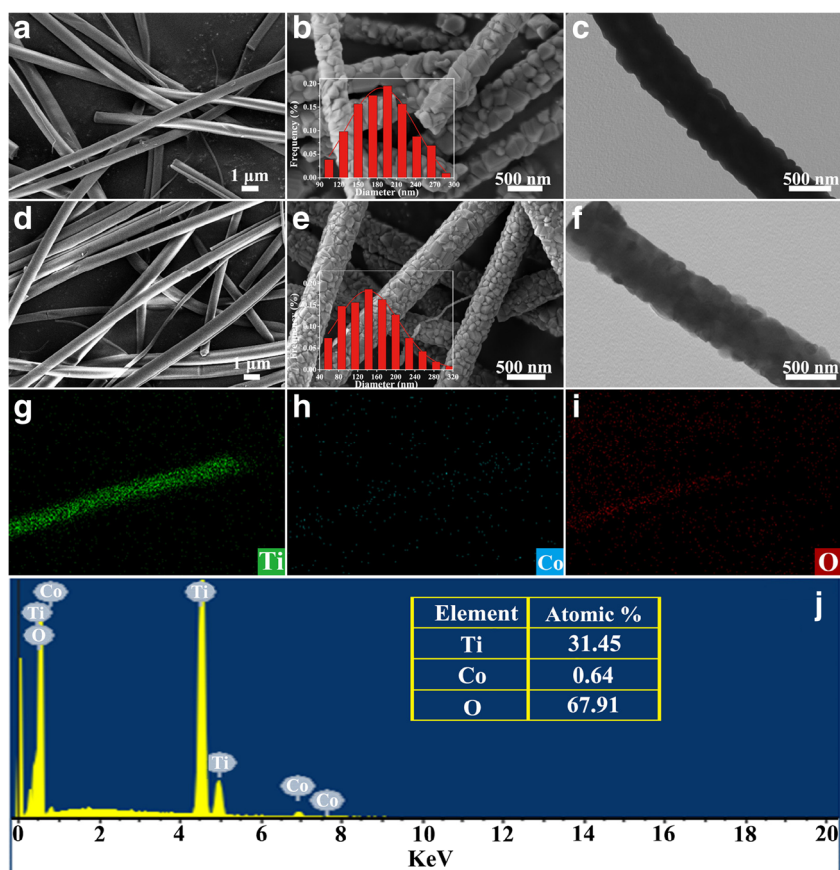


Fig. 3 **a, d** The representative SEM images of pure LTO and Co^{2+} -doped LTO precursor nanofibers, respectively. Typical SEM (**b, e**) and TEM (**c, f**) images of pure LTO and Co^{2+} -doped LTO nanofibers calcined at $800\text{ }^\circ\text{C}$ for 3 h, respectively. Insets of **b** and **e** are the particle size distribution curves. Corresponding EDS mappings (**g–i**) and EDS (**j**) of Co^{2+} -doped LTO nanofibers

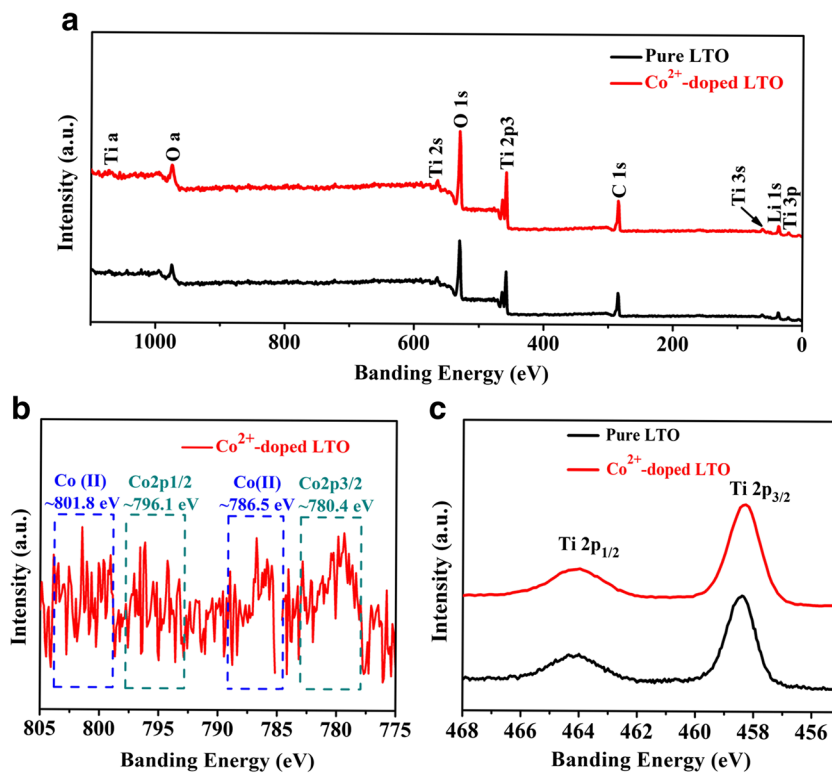


In order to further determine the chemical compositions of pure LTO and Co^{2+} -doped LTO nanofibers, XPS measurements in Fig. 4 were carried out in region of 0–1100 eV. A full XPS survey shows the presence of Li, Ti, and O elements for Co^{2+} -doped LTO nanofibers, but it is not evident that Co 2p peaks of Co^{2+} -doped LTO nanofibers appear in the range of 775 to 805 eV (Fig. 4a). To affirm the existence of Co element, the typical high-resolution XPS spectrum of Co 2p is shown in Fig. 4b. The weak binding energy peaks at ~ 796.1 and ~ 780.4 eV correspond to Co 2p_{1/2} and Co 2p_{3/2} [30], while the satellite peaks at ~ 801.8 and ~ 786.5 eV could be attributed to Co(II) oxide [31]. The formation of Co^{3+} ions for Co^{2+} -doped LTO nanofibers results from the oxidation of original Co^{2+} ions at high calcination temperature under air atmosphere. The high-resolution XPS spectra of Ti 2p are shown in Fig. 4c. Two broad peaks of pure LTO and Co^{2+} -doped LTO nanofibers at 464.2 and 458.4 eV correspond well with Ti 2p_{1/2} and Ti 2p_{3/2} peaks of Ti^{4+} ions, respectively. As a matter of fact, the radius of Co^{3+} ions (0.630 Å) is smaller than that of Co^{2+} ions (0.745 Å), so the enlarged lattice parameters (shown in Fig. 2c, d) could mainly result from the existence of Co^{2+} ions.

Potential capacity curves (Fig. 5a, b) and rate cycling performance (Fig. 5c) for pure LTO and Co^{2+} -doped LTO electrodes were tested between 1.0 and 2.5 V at 0.1, 0.2, 0.5, 1, 2,

and 5 C (1 C = 175 mA g^{-1}), respectively. As shown in Fig. 5a, the discharge capacity of pure LTO electrode reaches 170.9, 157.3, 143.1, 126.9, 110.6, and 78.9 mAh g^{-1} at 0.1, 0.2, 0.5, 1, 2, and 5 C, respectively. Furthermore, the capacity decreases rapidly and the separation between charge and discharge plateaus (ΔV) becomes large, accompanying with the increasing of current rates, which results from the low electronic conductivity and small Li^+ ions diffusion coefficient [32]. Figure 5b illustrates that the discharge capacity of Co^{2+} -doped LTO electrode could reach 172.4, 160.7, 151.3, 145.6, 141.1, and 138.1 mAh g^{-1} at 0.1, 0.2, 0.5, 1, 2, and 5 C, respectively, indicating that the introduction of Co^{2+} ions improves the discharge capacity of LTO electrode. As shown in Fig. 5c, the rate cycling performance of pure LTO and Co^{2+} -doped LTO electrodes was measured between 1.0 and 2.5 V at 0.2, 0.5, 1, 2, and 5 C, respectively. With the increase of C rate, Co^{2+} -doped LTO electrode performs the better rate cycling performance than pure LTO electrode. Even at the high rate of 5 C, the average discharge capacity of Co^{2+} -doped LTO electrode could still maintain as high as 138 mAh g^{-1} . In order to thoroughly investigate the cycling stability under the high rate for the pure LTO and Co^{2+} -doped LTO electrodes, the cycling performance of pure LTO and Co^{2+} -doped LTO electrodes was tested between 1.0 and 2.5 V at 5 C for 200 cycles. As shown in Fig. 5d, both pure LTO and Co^{2+} -doped LTO

Fig. 4 **a** XPS survey spectra of pure LTO and Co^{2+} -doped LTO nanofibers. **b** Typical high-resolution XPS spectrum of Co^{2+} -doped LTO nanofibers at the range of 775 to 805 eV. **c** Typical high-resolution XPS spectra of Ti 2p of pure LTO and Co^{2+} -doped LTO nanofibers



electrodes perform the admirable cycling stability with scarcely any capacity loss at 5 C after 200 cycles. Especially, Co^{2+} -doped LTO electrodes have the high discharge capacity (140.1 mAh g^{-1}) and still remain at 136.5 mAh g^{-1} after 200 cycles at 5 C.

Figure 6 exhibits the cyclic voltammograms of pure LTO and Co^{2+} -doped LTO electrodes between 1.0 and 2.5 V at a scan rate of 0.2, 0.4, 0.6, 0.8, and 1.0 mV s^{-1} . There exists a pair of cathodic/anodic peaks at $\sim 1.5 \text{ V}/1.7 \text{ V}$ with the different scan rate of each

Fig. 5 **a–b** Potential capacity curves of pure LTO and Co^{2+} -doped LTO electrodes between 1.0 and 2.5 V at 0.1, 0.2, 0.5, 1, 2, and 5 C ($1 \text{ C} = 175 \text{ mA g}^{-1}$), respectively. **c** The rate cycling performance of pure LTO and Co^{2+} -doped LTO electrodes between 1.0 and 2.5 V at 0.1, 0.2, 0.5, 1, 2, and 5 C, respectively. **d** The cycling performance of pure LTO and Co^{2+} -doped LTO electrodes between 1.0 and 2.5 V at 5 C for 200 cycles.

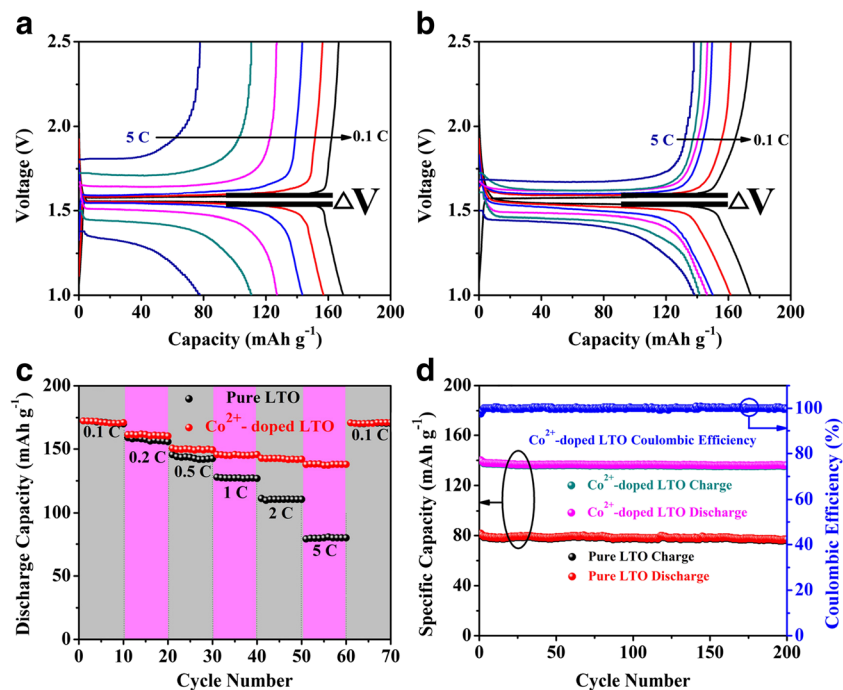
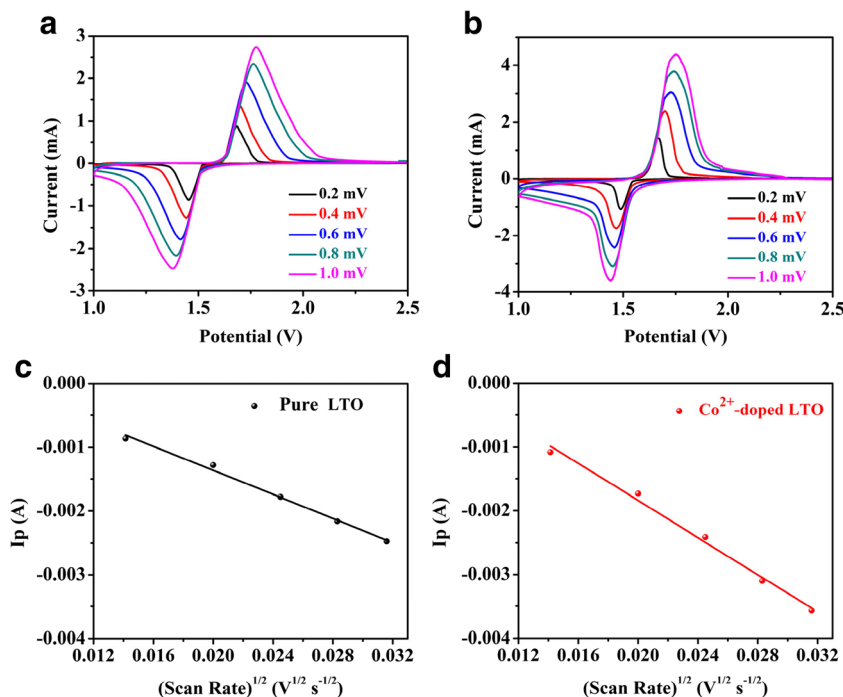


Fig. 6 **a, b** The cyclic voltammograms of pure LTO and Co^{2+} -doped LTO electrodes between 1.0 and 2.5 V at a scan rate of 0.2, 0.4, 0.6, 0.8, and 1.0 mV s^{-1} , respectively. **c, d** The relationship between the peak current (I_p) and square root of scan rate ($v^{1/2}$) cathodic process of pure LTO and Co^{2+} -doped LTO electrodes, respectively



sample, which corresponds to the reversible change of Ti^{4+} to Ti^{3+} during the charge/discharge process accompanied by the insertion of Li^+ ions. The φ_a (anodic peak) and φ_c (cathodic peak) of pure LTO electrodes are 1.453/1.683, 1.442/1.698, 1.415/1.728, 1.394/1.763, and 1.377/1.776 V at a scan rate of 0.2, 0.4, 0.6, 0.8, and 1.0 mV s^{-1} , respectively, while the φ_a and φ_c of Co^{2+} -doped LTO electrode are 1.488/1.668, 1.467/1.669, 1.458/1.728, 1.450/1.742, and 1.440/1.753 V at a scan rate of 0.2, 0.4, 0.6, 0.8, and 1.0 mV s^{-1} , respectively. The corresponding potential difference $\Delta\varphi$ ($\varphi_a - \varphi_c$) of pure LTO and Co^{2+} -doped LTO electrodes is 230/180, 256/232, 313/270, 369/292, and 399/313 mV, respectively. Moreover, the potential difference of CV peaks reflects the polarization degree of the electrodes [33]. It is obvious that Co^{2+} -doped LTO electrode has the lower polarization degree than pure LTO electrode.

As shown in Fig. 8c, the relationship between the peak current (V) and square root of scan rate ($\text{V}^{1/2} \text{s}^{-1/2}$) can be

used to evaluate the Li^+ diffusion coefficients for pure LTO and Co^{2+} -doped LTO electrodes. On the basis of CV data and following Eq. [34]:

$$I_p = 2.69 \times 10^5 A n^{3/2} C_0 D^{1/2} v^{1/2} \quad (1)$$

where D is the Li^+ diffusion coefficient, A is the surface area of the electrode (1.13 cm^2), n is the number of electrons during the half-reaction of the redox couple, and C_0 the is molar concentration of Li^+ in solid; so the conclusion could be obtained as follows:

$$I_p/v^{1/2} \propto D^{1/2}$$

Therefore, the Li^+ ion diffusion coefficient of Co^{2+} -doped LTO electrode is higher than that of pure LTO electrode, indicating that Co^{2+} ion doping could enhance the diffusion coefficient of Li^+ ions.

The electrochemical impedance spectra (EIS) of pure LTO and Co^{2+} -doped LTO electrodes between 1.0 and 2.5 V at 5 C

Fig. 7 **a** The electrochemical impedance spectra of pure LTO and Co^{2+} -doped LTO electrodes between 1.0 and 2.5 V at 5 C after 200 cycles (measured in the frequency range from 0.01 Hz to 100 kHz), and inset shows the equivalent circuit. **b** Inclined lines of the EIS in the low-frequency region

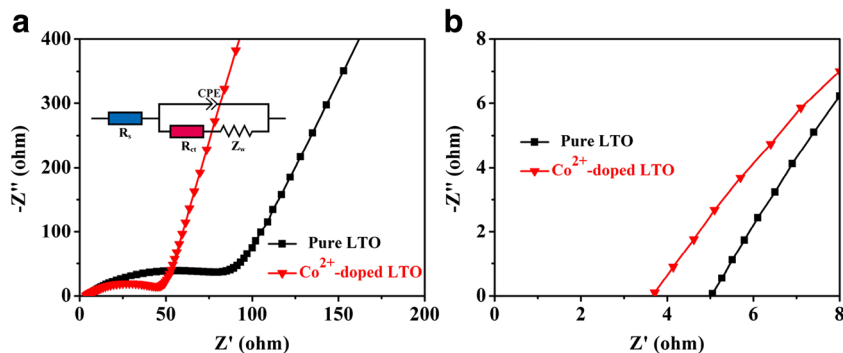
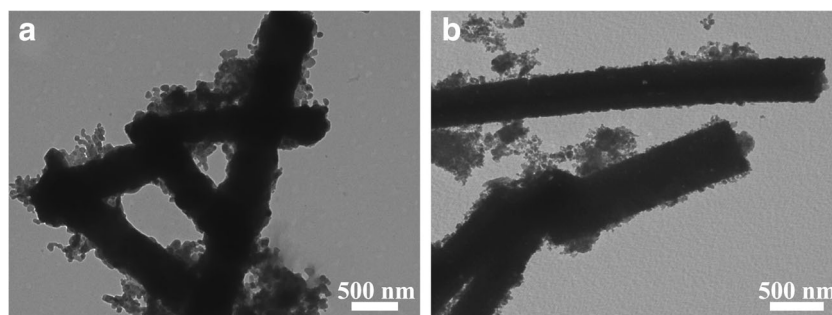


Fig. 8 TEM images of pure LTO (a) and Co^{2+} -doped LTO (b) electrodes after 200 cycles between 1.0 and 2.5 V at 5 C, respectively



were further measured after 200 cycles in the frequency range from 0.01 Hz to 100 kHz, respectively. According to the equivalent circuit (inset of Fig. 7a), the EIS are fitted successfully. As shown in Fig. 7a, the electrochemical impedance spectra consist of one high-to-medium-frequency semicircle and one low-frequency straight line, which are mainly related to the charge transfer resistance and Warburg impedance, respectively [35]. Comparing with pure LTO electrode, Co^{2+} -doped LTO electrode possesses the reduced charge transfer resistance, which could result in the enhanced electrochemical performance (Fig. 7a, b). The possible reasons for this are as follows: First of all, Co^{2+} ion doping can increase the electronic conductivity of LTO electrode. Moreover, the introduction of Co^{2+} ions enlarges the lattice volume of LTO, which could improve the lithium insertion/extraction kinetics during the charge/discharge process. Last but not the least, the reduced nanoparticle size of Co^{2+} -doped LTO nanofibers may be also the reason for enhancing the lithium insertion/extraction kinetics by providing the rapid and efficient pathways for ion and electron transport.

The coin cells were disassembled after 200 cycles between 1.0 and 2.5 V at 5 C to track the structural stability of 1D nanofibers during the high-rate charge/discharge process. The active materials are then peeled off from Cu foil and calcined at 500 °C for 2 h in the air atmosphere in order to burn off the acetylene black and the polytetrafluoroethylene. As shown in Fig. 8, the appearance of 1D nanostructure for pure LTO and Co^{2+} -doped LTO electrodes further exhibits the relatively high structural stability, especially at a high current density.

Conclusions

In conclusion, this work reported a novel and maneuverable Co^{2+} doping strategy for LTO nanofibers. The introduction of Co^{2+} ions greatly improved the rate performance and cycling stability of LTO anode materials. When all is said and done, the high-rate and high-capacity lithium storage could be attributed to the enhanced electrical conductivity and the rapid and efficient pathways for ion and electron transport. The superior electrochemistry performances proved that the

Co^{2+} -doped LTO electrode could have a great potential as LIBs anode materials.

Funding information This work was supported by the Shandong Provincial Natural Science Foundation (Grant No. ZR2016BM22) and Science and Technology Program of Shandong Province (Grant No. 2014GGX102039).

Compliance with ethical standards

Conflict of interest The authors declare that they have no conflict of interest.

References

- Scrosati B, Hassoun J, Sun YK (2011) Lithium-ion batteries. A look into the future. *Energy Environ Sci* 4(9):3287–3295. <https://doi.org/10.1039/c1ee01388b>
- Kundu D, Talaie E, Duffort V, Nazar LF (2015) The emerging chemistry of sodium ion batteries for electrochemical energy storage. *Angew Chem Int Ed* 54(11):3431–3448. <https://doi.org/10.1002/anie.201410376>
- Jeong G, Kim YU, Kim H, Kim YJ, Sohn HJ (2011) Prospective materials and applications for Li secondary batteries. *Energy Environ Sci* 4(6):1986–2002. <https://doi.org/10.1039/c0ee00831a>
- He YB, Liu M, Huang ZD, Zhang B, Yu Y, Li B, Kang F, Kim JK (2013) Effect of solid electrolyte interface (SEI) film on cyclic performance of $\text{Li}_4\text{Ti}_5\text{O}_{12}$ anodes for Li ion batteries. *J Power Sources* 239:269–276. <https://doi.org/10.1016/j.jpowsour.2013.03.141>
- Sun Y, Zhao L, Pan H, Lu X, Gu L, Hu YS, Li H, Armand M, Ikuhara Y, Chen L, Huang X (2013) Direct atomic-scale confirmation of three-phase storage mechanism in $\text{Li}_4\text{Ti}_5\text{O}_{12}$ anodes for room-temperature sodium-ion batteries. *Nat Commun* 4:1–10
- Shen LF, Zhang XG, Uchaker E, Yuan CZ, Cao GZ (2012) $\text{Li}_4\text{Ti}_5\text{O}_{12}$ nanoparticles embedded in a mesoporous carbon matrix as a superior anode material for high rate lithium ion batteries. *Adv Energy Mater* 2(6):691–698. <https://doi.org/10.1002/aenm.201100720>
- Zhang Q, Lu HS, Zhong H, Yan XD, Ouyang C, Zhang L (2015) W^{6+} & Br^- codoped $\text{Li}_4\text{Ti}_5\text{O}_{12}$ anode with super rate performance for Li-ion batteries. *J Mater Chem A* 3(26):13706–13716. <https://doi.org/10.1039/C5TA02784E>
- Zhu GN, Wang YG, Xia YY (2012) Ti-based compounds as anode materials for Li-ion batteries. *Energy Environ Sci* 5(5):6652–6667. <https://doi.org/10.1039/c2ee03410g>
- Zhang YL, Lin ZJ, Hu XB, Cao P, Wang YQ (2016) One-step solid-state synthesis of $\text{Li}_4\text{Ti}_5\text{O}_{12}/\text{C}$ with low in situ carbon content and

- high rate cycling performance. *J Solid State Electrochem* 20(1): 215–223. <https://doi.org/10.1007/s10008-015-3019-0>
10. Kim J, Kim JY, Pham-Cong D, Jeong SY, Chang J, Choi JH, Braun PV, Cho CR (2016) Individually carbon-coated and electrostatic-force-derived graphene-oxide-wrapped lithium titanium oxide nanofibers as anode material for lithium-ion batteries. *Electrochim Acta* 199:35–44. <https://doi.org/10.1016/j.electacta.2016.03.137>
 11. Zhao Z, Xu YL, Ji MD, Zhang H (2013) Synthesis and electrochemical performance of F-doped $\text{Li}_4\text{Ti}_5\text{O}_{12}$ for lithium-ion batteries. *Electrochim Acta* 109:645–650. <https://doi.org/10.1016/j.electacta.2013.07.164>
 12. Zou HL, Liang X, Feng XY, Xiang HF (2016) Chromium-modified $\text{Li}_4\text{Ti}_5\text{O}_{12}$ with a synergistic effect of bulk doping, surface coating, and size reducing. *ACS Appl Mater Interfaces* 8(33):21407–21416. <https://doi.org/10.1021/acsami.6b07742>
 13. Jung JW, Lee CL, Yu S, Kim ID (2016) Electrospun nanofibers as a platform for advanced secondary batteries: a comprehensive review. *J Mater Chem A* 4(3):703–750. <https://doi.org/10.1039/C5TA06844D>
 14. Hwang SM, Lim YG, Kim JG, Heo YU, Lim JH, Yamauchi Y, Park MS, Kim YJ, Dou SX, Kim JH (2014) A case study on fibrous porous SnO_2 anode for robust, high-capacity lithium-ion batteries. *Nano Energy* 10:53–62. <https://doi.org/10.1016/j.nanoen.2014.08.020>
 15. Kim KJ, Lee SW, Yim T, Kim JG, Choi JW, Kim JH, Park MS, Kim YJ (2014) A new strategy for integrating abundant oxygen functional groups into carbon felt electrode for vanadium redox flow batteries. *Sci Rep* 4:6906–6912
 16. Jeong G, Kim JG, Park MS, Soo MH, Hwang SM, Kim YU, Kim YJ, Kim JH, Dou SX (2014) Core-shell structured silicon nanoparticles@ TiO_2 /carbon mesoporous microfiber composite as a safe and high-performance lithium-ion battery anode. *ACS Nano* 8(3):2977–2985. <https://doi.org/10.1021/nn500278q>
 17. Li D, Lu QF, Guo EY, Wei MZ, Xiu ZL, Ji XY (2017) Graphene membrane encapsulated Co_3O_4 nanotubes with superior capacity and stability as anode materials for lithium ion batteries. *J Sol-Gel Sci Technol* 82(1):75–84. <https://doi.org/10.1007/s10971-016-4274-y>
 18. Rui XH, Tang YX, Malyid OI, Gusake A, Zhang YY, Niu ZQ, Tan HT, Persson C, Chen XD, Chen Z, Yan QY (2016) Ambient dissolution-recrystallization towards large-scale preparation of V_2O_5 nanobelts for high-energy battery applications. *Nano Energy* 22:583–593. <https://doi.org/10.1016/j.nanoen.2016.03.001>
 19. Zhang YY, Zhang CM, Lin Y, Xiong DB, Wang D, Wu XY, He DN (2014) Influence of Sc^{3+} doping in B-site on electrochemical performance of $\text{Li}_4\text{Ti}_5\text{O}_{12}$ anode materials for lithium-ion battery. *J Power Sources* 250:50–57. <https://doi.org/10.1016/j.jpowsour.2013.10.137>
 20. Cai YJ, Huang YD, Jia W, Zhang Y, Wang XC, Guo Y, Jia DZ, Pang WK, Guo ZP, Wang LS (2016) Two-dimensional dysprosium-modified bamboo-slip-like lithium titanate with high-rate capability and long cycle life for lithium-ion batteries. *J Mater Chem A* 4(45): 17782–17790. <https://doi.org/10.1039/C6TA06956H>
 21. Li ZY, Li JL, Zhao YG, Yang K, Gao F, Li X (2016) Structure and electrochemical properties of Sm-doped $\text{Li}_4\text{Ti}_5\text{O}_{12}$ as anode material for lithium-ion batteries. *RSC Adv* 19:15492–15500
 22. Guo QJ, Wang Q, Chen G, Li B (2016) Multigrain electrospun nickel doped lithium titanate nanofibers with high power lithium ion storage. *J Mater Chem A* 72:11–23
 23. Kim JG, Park MS, Hwang SM, Heo YU, Liao T, Sun ZQ, Park JH, Kim KJ, Jeong G, Kim YJ, Kim JH, Dou SX (2014) Zr^{4+} doping in $\text{Li}_4\text{Ti}_5\text{O}_{12}$ anode for lithium-ion batteries: open Li^+ diffusion paths through structural imperfection. *ChemSusChem* 7(5):1451–1457. <https://doi.org/10.1002/cssc.201301393>
 24. Ge YQ, Jiang H, Fu K, Zhang CH, Zhu JD, Chen C, Lu Y, Qiu YP, Zhang XW (2014) Copper-doped $\text{Li}_4\text{Ti}_5\text{O}_{12}$ /carbon nanofiber composites as anode for high-performance sodium-ion batteries. *J Power Sources* 272:860–865. <https://doi.org/10.1016/j.jpowsour.2014.08.131>
 25. Kotnana G, Jammalamadaka SN (2015) General structure analysis system (GSAS). *J Appl Phys* 117:562
 26. Toby BH (2001) EXPGUI, a graphical user interface for GSAS. *Appl Crystallogr* 34(2):210–213. <https://doi.org/10.1107/S0021889801002242>
 27. Liu XN, Lu QF, Liu JH (2016) Electrospinning preparation of one-dimensional $\text{ZnO}/\text{Bi}_2\text{WO}_6$ heterostructured sub-microbelts with excellent photocatalytic performance. *J Alloy Compd* 662:598–606. <https://doi.org/10.1016/j.jallcom.2015.12.050>
 28. Song H, Yun SW, Chun HH, Kim MG, Chung KY, Kim HS, Cho BW, Kim YT (2012) Anomalous decrease in structural disorder due to charge redistribution in Cr-doped $\text{Li}_4\text{Ti}_5\text{O}_{12}$ negative-electrode materials for high-rate Li-ion batteries. *Energy Environ Sci* 5(12): 9903–9913. <https://doi.org/10.1039/c2ee22734g>
 29. Yeo Y, Jung JW, Park K, Kim ID (2015) Graphene-wrapped anatase TiO_2 nanofibers as high-rate and long-cycle-life anode material for sodium ion batteries. *Sci Rep* 5(1):13862–13869. <https://doi.org/10.1038/srep13862>
 30. Chen CC, Huang YN, Zhang H, Wang XF, Wang YJ, Jiao LF, Yuan HT (2016) Controllable synthesis of Cu-doped CoO hierarchical structure for high performance lithium-ion battery. *J Power Sources* 314:66–75. <https://doi.org/10.1016/j.jpowsour.2016.02.085>
 31. Xiao JW, Chen C, Xi JB, Xu YY, Xiao F, Wang S, Yang SH (2015) Core-shell $\text{Co}@\text{Co}_3\text{O}_4$ nanoparticle-embedded bamboo-like nitrogen-doped carbon nanotubes (BNCNTs) as a highly active electrocatalyst for the oxygen reduction reaction. *Nano* 7:7056–7064
 32. Cui K, Hu SC, Li YK (2016) Nitrogen-doped graphene-decorated LiVPO_4F nanocomposite as high-voltage cathode material for rechargeable lithium-ion batteries. *J Power Sources* 325:465–473. <https://doi.org/10.1016/j.jpowsour.2016.06.058>
 33. Wu N, Yang ZZ, Yao HR, Yin YX, Gu L, Guo YG (2015) Improving the electrochemical performance of the $\text{Li}_4\text{Ti}_5\text{O}_{12}$ electrode in a rechargeable magnesium battery by lithium-magnesium co-intercalation. *Angew Chem Int Ed* 54(19):5757–5761. <https://doi.org/10.1002/anie.201501005>
 34. Wang L, Xiao QZ, Wu LJ, Lei GT, Li ZH (2013) Spinel LiCrTiO_4 fibers as an advanced anode material in high performance lithium ion batteries. *Solid State Ionics* 236:43–47. <https://doi.org/10.1016/j.ssi.2013.01.018>
 35. Zhou XY, Tang JJ, Yang J, Xie J, Huang B (2013) Seaweed-like porous carbon from the decomposition of polypyrrole nanowires for application in lithium ion batteries. *J Mater Chem A* 1(16): 5037–5044. <https://doi.org/10.1039/c3ta10557a>